PNAS RESEARCH ARTICLE | IMMUNOLOGY AND INFLAMMATION
BIOPHYSICS AND COMPUTATIONAL BIOLOGY OPEN ACCESS

B cell receptors and free antibodies have different antigen-binding kinetics

Miguel García-Sánchez[a], Mario Castro[a,1], and José Faro[b,c,1]

Edited by Simon Fillatreau, INSERM, Paris, France; received December 5, 2022; accepted July 21, 2023, by Editorial Board Member Philippa Marrack

Since the pioneering works of Berg and Purcell, discriminating between diffusion followed by binding has played a central role in understanding cell signaling. B cell receptors (BCR) and antibodies (Ab) challenge that simplified view as binding to the antigen follows after a chain of diffusion and rotations, including whole molecule rotation and independent tilts and twists of their Fab arms due to their Y-shaped structure and flexibility. In this paper, we combine analytical calculations with Brownian simulations to derive the first-passage times due to these three rotations positioning the Fab paratopes at a proper distance and orientation required for antigen binding. Our results indicate that when measuring Ab–Ag effective kinetic binding rates, using experimental methods in which the analyte is in solution only gives values proportional to the intrinsic binding rates, k^+, and k^-, for values of k^+ up to 10^9 s^{-1}. Beyond that, a plateau of the effective 3D on rate between 10^8 $M^{-1}s^{-1}$ and 10^9 $M^{-1}s^{-1}$ is attained. Additionally, for BCR–Ag interactions, the effective 2D on and off binding rates can only be inferred from the corresponding effective 3D on and off rates for values of effective 3D on rates lower than 10^6 $M^{-1}s^{-1}$. This is highly relevant when trying to relate BCR–antigen-binding strength and B cell response, especially during germinal center reactions. Therefore, there is a pressing need to reexamine our current understanding of the BCR–antigen kinetic rates in germinal centers using the latest experimental assays for BCR–Ag interactions.

B cell receptor | humoral response | immunoglobulins | first-passage times | kinetic rates

Significance

In vivo, B cell receptor (BCR)–antigen interactions occur in a 2-dimensional (2D) environment with antigen anchored to a membrane. Conversely, antibody–antigen interactions typically occur in a 3-dimensional (3D) environment. The rotation necessary for the reactive sites (paratope in BCR and antibody and epitope in antigen) to align is a crucial factor in the binding reaction's kinetic rates, but its impact has been underestimated and currently is unknown. Combining theory and existing empirical data, our study provides the first estimation of approximate 2D and 3D global rotational rates of BCR and antibody paratopes and estimates of 2D and 3D effective kinetic rates based on intrinsic binding rates. Our work also allows to estimate unavailable 2D rates from existing 3D data.

Our understanding of antibody–antigen (Ab–Ag) interactions is based on decades of research on diffusion-limited reactions (1). When antigens bind to B cell receptors (BCRs), it triggers the antigen-specific activation of B lymphocytes, which then differentiate into antibody-secreting plasma cells. However, it is important to note that despite both being immunoglobulins (Ig), BCRs and antibodies (Abs) have distinct differences. BCRs are membrane-bound Igs with a tail that spans the B cell membrane into the cytoplasm, while Abs are soluble Ig isoforms that lack membrane anchoring and a transmembrane tail (2).

The basic structure of Igs consists of two identical Ag-binding arms or fragments (Fab) linked to a single constant arm (Fc) through an amino acid sequence called the hinge region (Fig. 1*A*), forming the familiar bivalent Y shape (2). Fab arms bind Ags through a small area at each free Fab end called paratope (*P*), and the specific Ag interface area involved in a Fab–Ag bond is called an epitope (*E*) (Fig. 1*A*). The length and flexibility of the hinge region linking Fab arms to the Fc arm are specific to each Ig isotype (3), allowing the two Fab arms to pivot independently of each other about the Fc region.

During the humoral immune response to protein antigens (Ags), B cells engage with their cognate Ags present in immunocomplexes on the follicular dendritic cell (FDC) membrane (4–6), which occurs in a 2-dimensional (2D) setting (7, 8). The understanding that ligand–receptor interactions in cell–cell adhesion occur in 2D has been established for some time (9), along with theoretical analyses of diffusion-driven receptor clustering in 2D (10–12). Over 20 y ago, it was proposed that BCR–Ag interactions in vivo primarily occur in 2D and exhibit distinct kinetic rates compared to humoral Ab–Ag interactions (13). Similar 2D interactions exist in systems involving cell adhesion molecules and T cell receptor–peptide-major histocompatibility complex (TCR-pMHC) interactions (14–16). However, the 2D kinetic and affinity constants for BCR–Ag interactions have yet to be measured.

Building upon the research of DeLisi (17), we previously demonstrated that protein–protein interactions can be thoroughly understood through three sequential processes: translational diffusion, rotational diffusion, and molecular binding. This has been reviewed in ref. 7. In 2D conditions for BCR–Ag interactions and 3D conditions for

Author contributions: M.C. and J.F. designed research; M.G.-S. performed all the stochastic simulations; all authors performed research, analyzed data and wrote the paper.

The authors declare no competing interest.

This article is a PNAS Direct Submission. S.F. is a guest editor invited by the Editorial Board.

[1]To whom correspondence may be addressed. Email: jfaro@uvigo.es or marioc@comillas.edu.

This article contains supporting information online at https://www.pnas.org/lookup/suppl/doi:10.1073/pnas.2220669120/-/DCSupplemental.

Published August 24, 2023.

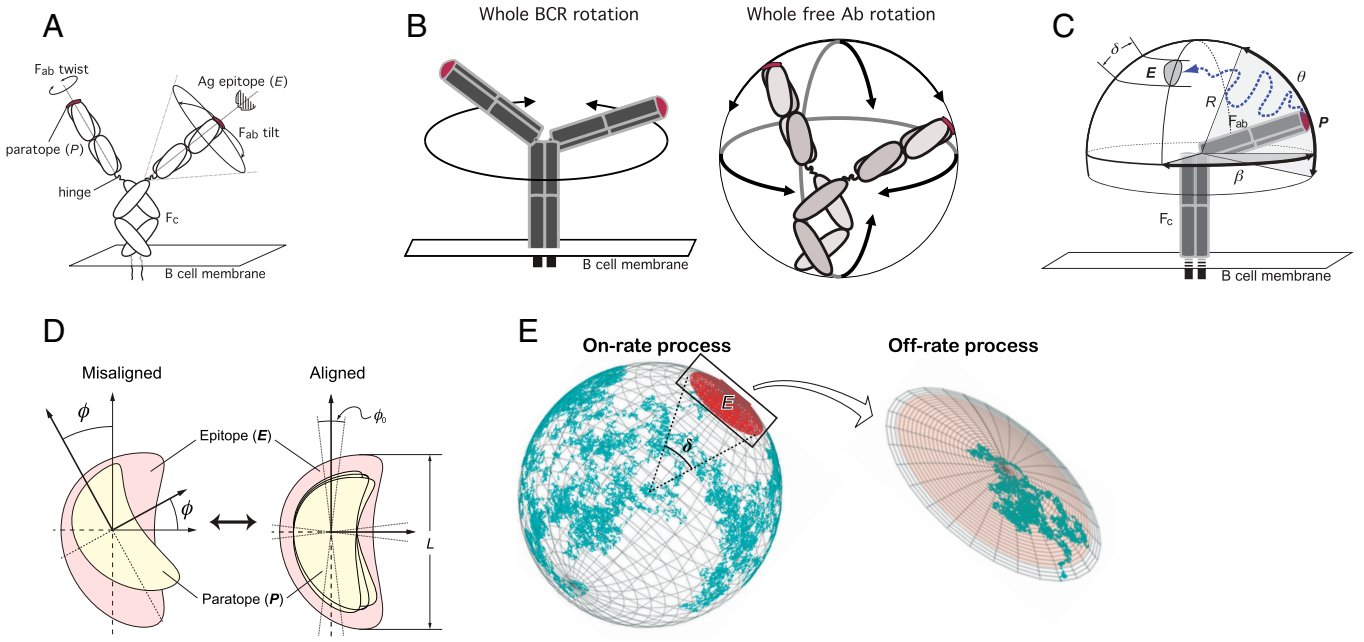

Fig. 1. Possible Ig rotations impacting on the position of a paratope *P* relative to an Ag epitope *E*. (*A*) The position of each paratope in an Ig (whether membrane-immunoglobulin, mIg, or free antibody, Ab) is independently submitted to two possible Fab rotations, Fab tilt (wagging and wobbling; depicted on the *Right* side) and Fab twist in which each Fab arm rotates along its major axis (from the hinge region to *P*; depicted on the *Left* side). The speed of these two Fab rotations might differ in BCRs and free Abs. (*B*) The position of each paratope is also affected by the rotation of the whole Ig. The *Left* side depicts BCR whole rotation, mostly restricted to a rotation along the Fc axis. For clarity, in panels *A*–*C*, we have omitted the CD79 heterodimer, which is tightly associated with the BCRs' Fc membrane-proximal and transmembrane domains. The *Right* side depicts free Ab whole rotation, which is unrestricted in the three spatial dimensions. (*C*) Sketch of the diffusion of *P* due to Fab tilt, assuming the epitope is in a fixed position; this movement is constrained to a spherical cap on a sphere of radius R = length of a Fab arm ≈ 84 Å (21) and to Fab altitude and azimuth angles, respectively, θ (measured from the south pole of the sphere) and β (the azimuthal angle of the Fab measured from the location of the epitope). Depicted is a possible path followed by paratope *P* toward epitope *E* (dotted line). The angle δ corresponds to an arc on the spherical surface equal to the major length of *E*. For clarity, the outlined mIg is depicted with only one Fab arm. (*D*) Alignment or misalignment of *P* and *E* due to Fab twist. *P* rotates with variable angle ϕ relative to *E* (*Left* side). Such rotation will align or misalign *P* and *E*, allowing or impeding their chemical binding. For aligned *P* and *E*, there is a tolerance angle, ϕ_0, within which the chemical reaction can proceed (*Right* side). The view in panel *D* is along the major Fab axis. (*E*) Random Walk view of Igs' paratope diffusion. During the on-rate process, the center of mass of the paratope diffuses on the sphere (cyan broken line) until finding the epitope (red area); δ, the angle of the arc with a length equal to the major length of the epitope. During the off-rate process, the paratope's center of mass diffuses within the epitope area (pale red) until it escapes (gray area).

Ab–Ag interactions, the scaling properties of the translational on and off kinetic rates are similar, as reviewed in ref. 8. However, the global rotational on and off kinetic rates in both 2D and 3D conditions remain unknown. This raises questions about the limitations of effective 2D kinetic rates perceived by B cells and whether and under what circumstances the 2D BCR–Ag effective kinetic rates can be inferred from the 3D Ab–Ag effective kinetic rates.

Here, we perform a detailed analysis of BCR and Ab paratopes' rotational rates in 2D and 3D conditions, respectively, using the theory of stochastic narrow escape (18), and first passage processes (19). We combine existing experimental data with analytical calculations and Brownian simulations to provide a complete quantitative picture of the first-passage times associated with the BCR and Ab rotational degrees of freedom. Our results allowed us to estimate the effective on and off rotational rates, and hence, the effective 2D (BCR–Ag) and 3D (Ab–Ag) effective k^+ and k^- rate constants as a function of the intrinsic or molecular k^+ binding rate. Moreover, we could derive a formula relating the 2D effective kinetic rates to the corresponding 3D effective kinetic rates. Contrary to the traditional implicit assumption, this result indicates that the kinetics of BCR–Ag interactions can be inferred from those of 3D Ab–Ag interactions only for effective 3D on rates below a threshold close to 10^6 $M^{-1}s^{-1}$. Consequently, the kinetics of BCR–Ag interactions cannot be inferred, in general, from those of 3D Ab–Ag interactions.

A First-Passage-Time Formalism of the Rotational Diffusion Steps during BCR and Antibody Binding to Antigen

The Three-Step Description of Kinetic Binding. In general, the kinetics of reversible protein–protein interactions consist of three generic processes (mostly occurring sequentially): translation, rotation, and binding. Translational diffusion comprises the spatial approximation of *R* and *L* molecules to a distance that allows binding; we denote this close-enough by RL^*. In the second step, rotational diffusion, the two close molecules must attain a proper orientation to bind to each other; we denote this close and oriented state as *RL* (in the case of Igs, a paratope has to be properly oriented for binding its epitope). Once properly oriented, they can form a bound complex *C* (20). Eq. **1** summarizes these series of states and processes,

$$R + L \underset{k_d^-}{\overset{k_d^+}{\rightleftharpoons}} RL^* \underset{e^-}{\overset{e^+}{\rightleftharpoons}} RL \underset{k^-}{\overset{k^+}{\rightleftharpoons}} C \quad [1]$$

where k_d^+, k_d^- are, respectively, translational diffusion on and off rate constants, e^+ and e^- are diffusion on and off rate constants for effective or global rotation, and k^+ and k^- are the intrinsic or molecular on and off rate constants. It is worth noting that De Lisi (17) already emphasized the relevance of this three-step

analysis generalizing the diffusion only plus binding framework pioneered by Berg and Purcell (1).

Traditionally, binding has been analyzed experimentally, lumping together those three steps assuming they occur in a single step. The effective kinetic rates for this simplified view can be formally derived by assuming a quasi-steady state approximation for the intermediate states $[RL^*]$ and $[RL]$, which leads to the following expressions for k^+_{eff} and k^-_{eff} (7):

$$k^+_{\text{eff}} = \left.\frac{k^+_d\ e^+\ k^+}{k^-_d\ e^- + k^+(k^-_d + e^+)}\right|_{3D/2D} \quad [2]$$

$$k^-_{\text{eff}} = \frac{k^-_d\ e^-\ k^-}{k^-_d\ e^- + k^+(k^-_d + e^+)}\ |_{3D/2D}. \quad [3]$$

The subscripts $3D/2D$ denote that the translational and global rotational diffusion rate constants correspond to either 3D or 2D reactions. Note that k^+ and k^- are independent of the dimensional condition and, thus, are identical in 3D and 2D interactions. We have shown before that the divisor in these equations determines an observability threshold for k^+,

$$k^+_{\text{threshold}} = \frac{k^-_d\ e^-}{k^-_d + e^+}, \quad [4]$$

such that for $k^+ > k^+_{\text{threshold}}$, k^+_{eff} approaches asymptotically a plateau given by $k^+_{\text{plateau}} = \frac{k^+_d\ e^+}{k^-_d + e^+}$, and k^-_{eff} becomes proportional to the dissociation affinity constant (8).

This three-step process can be further analyzed to capture the subtle—yet crucial—role of the Y structure of BCRs and Abs. Due to thermal fluctuations, proteins diffuse randomly, driven by molecular collisions or vibrations, until that motion stops by reaching a binding site. In particular, the wagging and wobbling movements of Ig Fab arms relative to the Fc arm, made possible by the hinge region of the Ig heavy chains, determine the position of the corresponding paratopes relative to the Fc arm and are referred to here as tilt rotation of paratopes or Fab tilt (Fig. 1 *A* and *C*) (3, 22, 23). The on and off rate constants characterizing this rotation are denoted here e^+_t and e^-_t, respectively. In addition, a Fab arm can twist about its major axis thanks again to the relative flexibility of the hinge segment (24, 25). This Fab twisting contributes essentially to the orientation or alignment of a paratope relative to an epitope on a relatively immobile Ag molecule tethered to an FDC membrane. We refer to this rotation as alignment rotation (Fig. 1 *A* and *D*), and the on and off rate constants characterizing this rotation are denoted, respectively, e^+_a and e^-_a. Last, the possible rotation of the whole BCR about the Fc axis, like a spinning top, or the rotation of an Ab in solution as a whole (Fig. 1*B*) contributes to the global paratope rotation with on and off rate constants denoted e^+_w and e^-_w, respectively. Due to such a complex combination of different rotational diffusion modes affecting the relative position of paratopes of BCRs and free Abs, the above-mentioned global rate constants e^+ and e^- are, in fact, compound quantities of the more elemental rates characterizing the whole molecule, Fab tilt, and Fab alignment rotations.

The global on rotation takes place in two steps. First, once in the encounter state RL^*, a Fab paratope P can get close enough to an epitope E through whole Ig and Fab tilt rotation, a state denoted $[RL]$, and then P and E become correctly oriented by a twist or alignment rotation (RL state). The first step, the close approaching of P and E, combines the whole molecule and Fab tilt rotation processes taking place in parallel or in any temporal order. Hence, its rate is the sum of the two individual processes, $e^+_{w+t} = e^+_w + e^+_t$, and thus the corresponding mean time is given by $t_{w+t} = \frac{1}{e^+_{w+t}}$. However, the on alignment rotation follows sequentially after the approaching of P and E; hence, the mean rotation time of the two steps (approaching and alignment) is the sum of their respective mean times, that is, $t_{on} = t_{w+t} + t_a$ and, consequently, $\frac{1}{e^+} = \frac{1}{e^+_{w+t}} + \frac{1}{e^+_a}$. At variance with e^+, the RL state can revert to RL^* state either directly, by a combination of whole molecule and Fab tilt rotation processes (route 1), or through the intermediate $[RL]$ state (route 2). If the rate e^-_a is faster than e^-_{w+t}, then route 2 will dominate and the time it takes to go from RL state to RL^* state is essentially determined by the slower e^-_{w+t}; however, the same is true if e^-_a is slower than e^-_{w+t}, because then route 1 will dominate. In other words, the global off rotation rate, e^- (i.e., from the RL state to the RL^* state), is determined by the whole and tilt off rotations (which can take place in parallel or in any temporal order). This can be described in terms of the following reaction scheme:

$$\cdots \rightleftharpoons RL^* \underset{e^-_{w+t}}{\overset{e^+_{w+t}}{\rightleftharpoons}} [RL] \underset{e^-_a}{\overset{e^+_a}{\rightleftharpoons}} RL \rightleftharpoons \cdots \quad [5]$$

$$\longleftarrow\ e^-_{w+t}$$

And according to the above:

$$e^+ = \frac{e^+_{w+t} \times e^+_a}{e^+_{w+t} + e^+_a} \quad \text{and} \quad e^- = e^-_{w+t}. \quad [6]$$

In our calculations, we assume that the contribution of Ag to rotational rates is negligible compared to that of BCR or Ab (explained in *SI Appendix*, section F).

2D compound tilt+whole molecule rotational rates of BCRs. In BCRs, the anchoring to the cell membrane has two main effects related to the degrees of freedom of paratope movements. First, its whole rotation motion is restricted to essentially the axis normal to the cell membrane in a highly crowded molecular environment. Although the exact value of the whole BCR rotational diffusion coefficient, $D_w(2D)$, has not been experimentally determined, one can take as a reference value that of the epidermal growth factor receptor (26), which is of the order 10^3 rad^2/s. However, considering that EGFR in its native state is in a monomeric form with a single transmembrane domain and that BCRs have two transmembrane domains that are tightly associated with the transmembrane domains of the CD79 heterodimer, it can be safely assumed that the whole molecule rotation of BCRs is fairly slower than that of EGFR. Nevertheless, since $D_w(2D)$ of the EGFR is already three orders of magnitude smaller than the 2D tilt rotational diffusion coefficient $D_t(2D)$ (*SI Appendix*, Table S3) one has for BCRs $D_{w+t}(2D) \approx D_t(2D)$. Second, the Fab tilt flexibility determines the spherical surface domain Ω covered by paratopes (*SI Appendix*, Fig. S5). The different Ig isotypes and subclasses in humans and mice have different hinge regions, and consequently, they differ substantially in flexibility and tilt rotation. The flexibility in the polar angle θ, i.e., the flexibility of the Fab arms with respect to the Fc region (Fig. 1*C*), has been characterized (*SI Appendix*, section A and Table S1).

Contrary, the flexibility in the azimuthal angle β (Fig. 1*C*) is poorly characterized. Nevertheless, based on the study of Zhang et al. (27) that analyzed the conformational flexibility of IgG1 antibody molecules using individual particle electron tomography, one can argue that each paratope can cover a 180° range in the azimuthal angle. Thus, the total domain covered by both paratopes is $\Omega = \{(\theta, \beta)|\ \theta \in [\theta_{\min}, \theta_{\max}], \beta \in [0, 2\pi]\}$. Furthermore, since $D_t(2D) \gg D_w(2D)$, we can neglect the marginal effect of the whole rotation motion, i.e., $e^{2D\pm}_{t+w} \approx e^{2D\pm}_{t}$. In this approximation, each paratope covers one half of Ω, namely $\Omega_1 = \{(\theta, \beta)|\ \theta \in [\theta_{\min}, \theta_{\max}], \beta \in [0, \pi]\}$ and $\Omega_2 = \{(\theta, \beta)|\ \theta \in [\theta_{\min}, \theta_{\max}], \beta \in [\pi, 2\pi]\}$. For simplicity, we will suppose that the epitope is completely contained in either Ω_1 or Ω_2, and thus, we only need to consider one of both paratopes (*SI Appendix*, Fig. S5).

The mean on and off rotational times corresponding to the different rotational rate constants can be estimated using the theory of stochastic narrow escape (18) and first-passage processes (19) and are here denoted rotational mean first passage times (MFPT) (described in *SI Appendix*, sections B and C). Under the above definition of the domain Ω, the MFPTs depend on the initial position of the paratope (θ, β), and the epitope location θ_{epi} and size (δ; see Fig. 1 *C* and *E*).

Through Monte-Carlo simulations, we computed the global MFPT $\tau^{2D+}_t(\theta_{\text{epi}}, \delta)$ for the paratopes of the different IgGs subclasses, and for multiple values of $\delta = \{19°, 14°, 10°, 6°, 2°\}$ and different positions of the epitope measured by the arc length θ_{epi} (*SI Appendix*, Fig. S5). The results, summarized in Fig. 2, revealed conspicuous differences in the global MFPTs of the IgGs subclasses, being more notorious between the IgG2b and IgG1 subclasses. Note that we have presented our findings for a reference diffusivity $D = 1$ to highlight the comparison while disregarding specific diffusivity estimates. Actual times can be obtained by multiplying by the proper empirical diffusivity. Interestingly, the difference between IgGs subclasses increases as the size of the paratope δ decreases. In agreement with previous works (28), these results suggest that the same paratope in different Ab classes might result in different rotation rate constants and, therefore, in different effective rate constants, besides any differences imposed by Ig class-specific glycosylation (21, 29). The resulting tilt on rate is given by:

$$e^{2D+}_t = \frac{1}{\tau^{2D+}_t}, \qquad [7]$$

with τ^{2D+}_t given by *SI Appendix*, Eq. S19.

The off-rate process for BCRs is similar to that of soluble Abs, except that the whole rotational motion marginally contributes to the diffusion of the paratope. Therefore, the rotation off-rate $e^{2D-}_{t+w}(\delta) \approx e^{2D-}_{t}(\delta)$ is given by *SI Appendix*, Eq. S16 but with $D^{(2D)}_t$ instead of $D^{(2D)}_{t+w}$:

$$e^{2D-}_t(\delta) \approx \frac{8D^{(2D)}_t}{\sin^2 \delta/2}. \qquad [8]$$

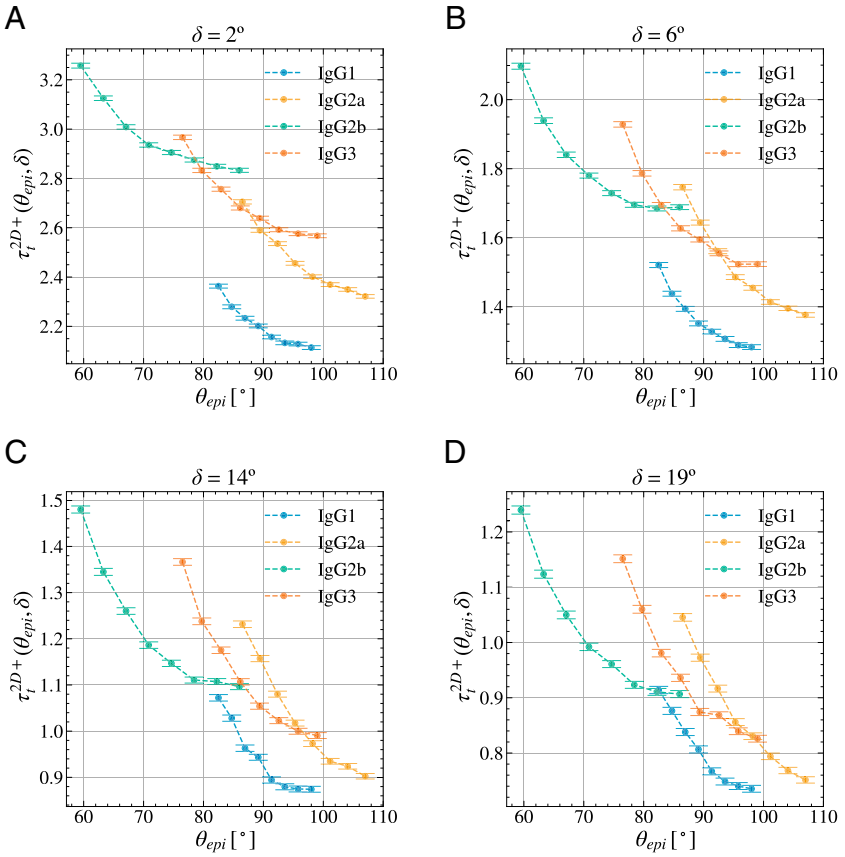

Fig. 2. Isotype Fab tilt flexibility affects the effective orientational rates. MFPT $\tau^{2D+}_t(\theta_{epi}, \delta)$ computed through Monte-Carlo simulations for the different mouse IgG subclasses and multiple values of θ_{epi} and δ. (*A*) $\delta = 2°$; (*B*) $\delta = 6°$; (*C*) $\delta = 14°$; (*D*) $\delta = 19°$. Parameters : $dt = 2 \cdot 10^{-4}$, $D = 1$, # initial positions = 3000, # repetitions per initial position = 100.

Estimates for the Rate Constants $k_d^{\pm}$ and $e^{\pm}$ in 2D and 3D and the Corresponding k^+ Threshold Values

Eqs. **2** and **3** allow connecting the underlying or intrinsic kinetic rates with the effective 2D and 3D ones. Thus, here, we integrate all the computations in the preceding sections. Calculations for k_d^+ and k_d^- can be found in ref. 8 and were performed using equations derived in Lauffenburger and Linderman (30) and experimentally derived diffusion coefficients for BCRs (31) and Abs (32). For the sake of comparison with the 3D case, units of k_d^+(2D) were transformed into $M^{-1}s^{-1}$ units following Lauffenburger and Linderman (30) as explained in *SI Appendix*, section H. However, to estimate the rate constants $e^{\pm}$, it is necessary to know, in addition to the angles ϕ_0 and δ, the rotational diffusion constants D_a, D_t, and D_w in 2D and 3D conditions. We calculated these constants based on experimental estimations of the corresponding mean rotational correlation times, denoted $t_{1\text{rad}}$, and *SI Appendix*, Eq. S23 (*SI Appendix*, section F). The values for $t_{1\text{rad}}$ corresponding to the three rotations considered here (whole molecule, tilt, and alignment) and/or the respective rotational diffusion constants, D_w, D_t, and D_a, estimated for Igs both in solution (3D) and attached to a large particle (2D) are summarized in *SI Appendix*, Table S3.

We can now go beyond qualitative arguments and calculate the global rotational kinetic rates, e^+ and e^-. For that, we first apply the estimations for the rotational diffusion constants in *SI Appendix*, Table S3 and for the angles ϕ_0 and δ (*SI Appendix*, section B) to *SI Appendix*, Eqs. S6, S12, S16, and S19, and then the resulting values are substituted in Eq. **6**. Ranges for the translational and global rotational kinetic rates in 2D and 3D conditions thus estimated, together with the corresponding threshold values for k^+ given by Eq. **4**, are summarized in *SI Appendix*, Table S3.

These results show that while k_d^+ and k_d^- have very different values from 2D to 3D conditions but similar scaling factors ($\sim 10^3$-fold), e^+ and e^- have similar values in 2D and 3D conditions, with e^- being twofold lower in 2D than in 3D. However, the most relevant here is that the k^+ threshold values differ by $\sim 10^3$-fold from 2D to 3D conditions. Hence, k^+_{plateau} for k^+_{eff}(2D) rates (BCR–Ag interactions) is much lower than for k^+_{eff}(3D) rates (free Ab–Ag interactions). More specifically, the 2D $k^+_{\text{threshold}}$ is $\leq 10^6$ s^{-1}, and for intrinsic binding rates k^+ larger than this threshold, k^+_{eff}(2D) rate approaches a plateau of $(1\text{-}2)\times 10^6$ $M^{-1}\,s^{-1}$. Hence, intrinsic k^+ rates higher than that threshold cannot have a differential impact on the effective binding rate of Ag to B cells. In contrast, the 3D $k^+_{\text{threshold}}$ is $\approx 5 \times 10^8\,s^{-1}$, and for values of the intrinsic binding rate k^+ larger than this threshold the k^+_{eff}(3D) rate plateaus between 5×10^8 and 5×10^9 $M^{-1}\,s^{-1}$ (Fig. 3, *Left*).

Upper Limits to the Effective Kinetic Rates of Ab– and BCR–Ag Interactions

The above estimations significantly impact our understanding of the effective kinetics of BCR–Ag and Ab–Ag interactions and their mutual relationship.

Already in the 1990s, some authors reported empirical observations indicating a ceiling for the k^+_{eff} of monoclonal Abs and their ligands [see for instance (33, 34)]. Calculations of the range for the k^+_{eff}(3D) plateau of Ab–Ag interactions help to explain it. This is illustrated in Fig. 3, *Left* side, where the mean variation of k^+_{eff}(3D) ±3 sd (solid lines) for increasing values of the intrinsic k^+ rate and the range of the corresponding plateaus (dashed red and blue lines) are plotted. In this figure, we also plot side by side with experimentally observed k^+_{eff}(3D) values for

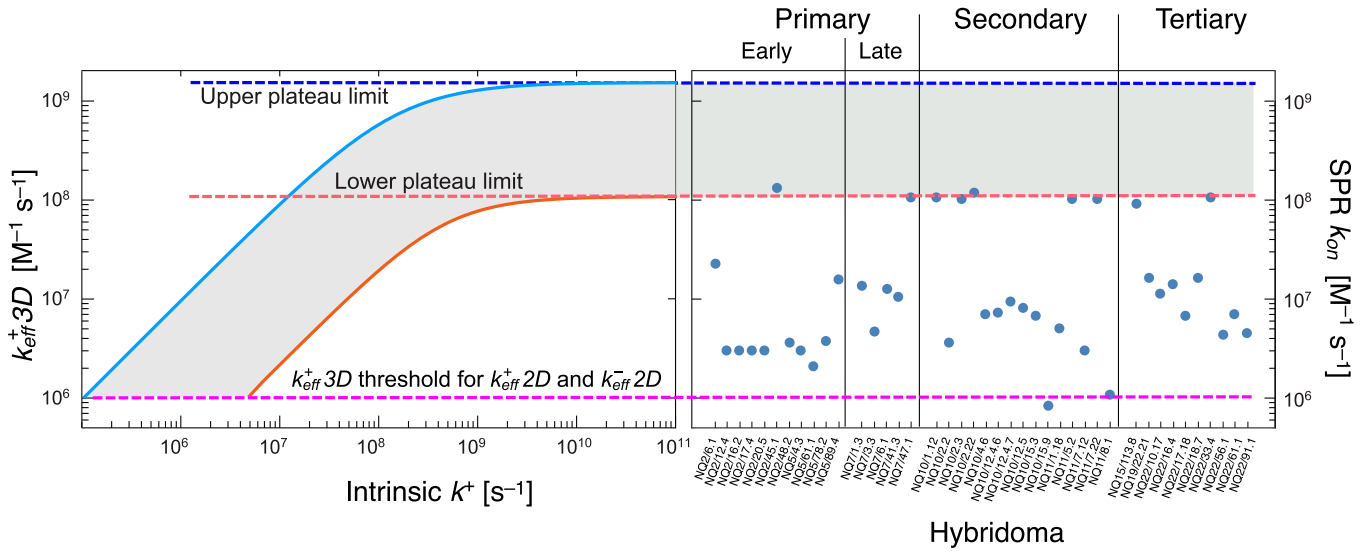

Fig. 3. Translational and rotational diffusion events put a limit to effective 3D on-rates. *Left* panel, theoretical estimation of k^+_{eff}(3D) for Ab–Ag interactions as a function of the intrinsic binding rate, k^+, based on Eq. **2**. Dashed blue and red lines correspond to *Upper* and *Lower* plateau boundaries. They are the mean ±3 sd of the distribution of plateau values obtained with 10^4 random sets of parameter values within the confidence limits of the 3D translational and rotational rates in Table 1. Blue and red curves were obtained with the parameters set used to estimate the *Lower* and *Upper* plateaus. The pink dashed line corresponds to the k^+_{eff}(3D) threshold for k^+_{eff}(2D) and k^-_{eff}(2D) depicted in Fig. 4, *Right* panel, Experimental 3D k_{on} values obtained with the SPR assay for different anti-2-PhOx monoclonal Abs (redrawn from ref. 33). Note the close agreement between the highest experimental values and our predicted k^+_{eff}(3D) lower plateau. Notice that all experimental values, from an early primary immune response to a tertiary immune response, lay within the k^+_{eff}(3D) *Lower* plateau and the k^+_{eff}(3D) threshold.

Table 1. Estimated ranges of translational and rotational diffusion rate constants for Igs in 2D and 3D conditions and the corresponding threshold values for k^+

	Translational diffusion		Rotational diffusion*		Threshold*
Isotype	k_d^+ ($M^{-1}\,s^{-1}$)	k_d^- (s^{-1})	e^+ (s^{-1})	e^- (s^{-1})	$\frac{k_d^- e^-}{(k_d^- + e^+)}$
2D	($\times 10^5$)	($\times 10^2$)	($\times 10^5$)	($\times 10^8$)	($\times 10^5$)
IgG1	8.8 to 29	8.3 to 27	11.6 to 14.7	3.2 to 4.9	1.8 to 11.5
IgG2a			10.6 to 13.4		2.0 to 12.5
IgG2b			9.0 to 11.2		2.4 to 14.8
IgG3			9.7 to 12.2		2.2 to 13.7
3D	($\times 10^8$)	($\times 10^5$)	($\times 10^5$)	($\times 10^8$)	($\times 10^8$)
IgG	3.8 to 34	5.3 to 72	9.4 to 13.6	6.7 to 12.7	1.9 to 11

*The procedure to obtain these ranges is described in *SI Appendix*, section G.

samples of monoclonal Abs obtained in primary, secondary, and tertiary murine immune responses against the hapten 2-phenyl-5-oxazolone (PhOx; Fig. 3, *Right* side, based on ref. 33).

Given that 2D $k^+_{\text{threshold}}$ and 2D k^+_{plateau} are at least 2 orders of magnitude lower than the corresponding 3D values, the 3D Ab–Ag effective affinity and rate constants cannot be used in general as surrogates for 2D BCR–Ag effective affinity and rate constants. However, this does not mean they cannot be used in all cases. For instance, for values of intrinsic $k^+ < 10^6\ s^{-1}$ $k^+_{\text{eff}}(3D)$ and $k^-_{\text{eff}}(3D)$ rates are close to the expected $k^+_{\text{eff}}(2D)$ and $k^-_{\text{eff}}(2D)$ rates, respectively. This can be shown to be the case by expressing $k^+_{\text{eff}}(2D)$ and $k^-_{\text{eff}}(2D)$ as a function of $k^+_{\text{eff}}(3D)$ (*SI Appendix*, section E).

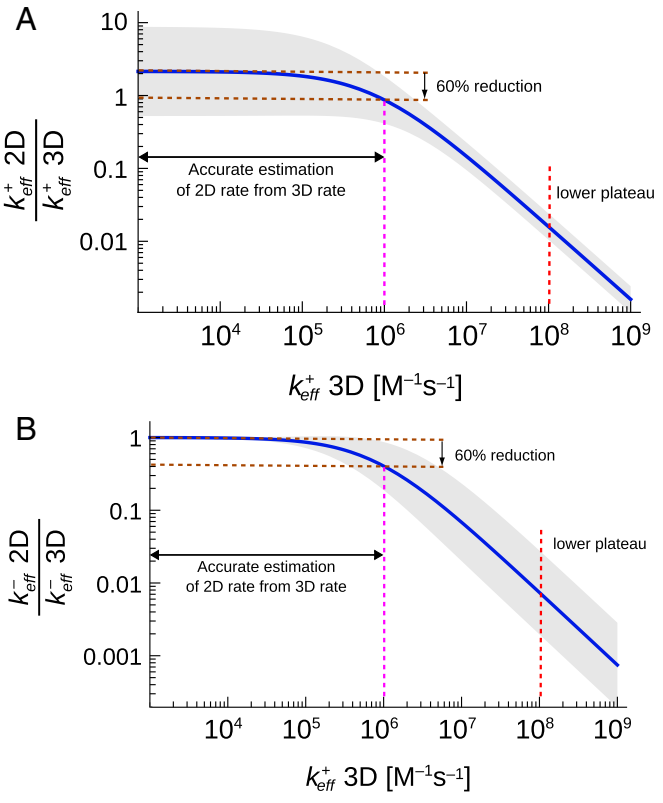

Fig. 4. 3D Effective on-rate observability thresholds for estimating 2D effective on and off rates using *SI Appendix*, Eqs. S21 and S22. Blue solid lines, variation of the ratios $k^+_{\text{eff}}(2D)/k^+_{\text{eff}}(3D)$ (*A*) and $k^-_{\text{eff}}(2D)/k^-_{\text{eff}}(3D)$ (*B*) as a function of $k^+_{\text{eff}}(3D)$. Each of these curves is an average from a distribution of curves obtained with the same 10^4 random sets of parameter values used in Fig. 3. Gray areas correspond to curves within the mean ±2 sd. A $k^+_{\text{eff}}(3D)$ threshold for each curve was defined as the $k^+_{\text{eff}}(3D)$ value for which a 60% reduction is obtained. This threshold is $10^6\ M^{-1}s^{-1}$ for both ratios, and it is indicated with a pink dashed line. For comparison, a red dashed line corresponding to the $k^+_{\text{eff}}(3D)$ *Lower* plateau in Fig. 3 is also depicted.

Plotting the ratios $k^+_{\text{eff}}(2D)/k^+_{\text{eff}}(3D)$ and $k^-_{\text{eff}}(2D)/k^-_{\text{eff}}(3D)$ as a function of $k^+_{\text{eff}}(3D)$ (Fig. 4) shows that $k^+_{\text{eff}}(3D)$ is a moderately reasonable proxy of $k^+_{\text{eff}}(2D)$ only for values of $k^+_{\text{eff}}(3D) \leq 4.4 \times 10^5\ M^{-1}\,s^{-1}$. At that value, $k^+_{\text{eff}}(2D)$ is in the range of 59% to 80% of $k^+_{\text{eff}}(3D)$. However, $k^-_{\text{eff}}(3D)$ is a reasonable proxy of $k^-_{\text{eff}}(2D)$ for values of $k^+_{\text{eff}}(3D) \leq 8 \times 10^5\ M^{-1}\,s^{-1}$ (at which value $k^-_{\text{eff}}(2D)$ is in the range of 57% to 80% of $k^-_{\text{eff}}(3D)$). These are very important results as they establish the approximate limits up to which the 3D kinetic rates of Ab–Ag binding provide values close to the expected BCR–Ag 2D kinetic rates.

Discussion and Conclusions

During B cell–FDC interactions, BCRs bind cognate Ag tethered on FDCs' membrane (4–6, 35) and hence in 2D conditions. In contrast, in in vitro assays, Ab–Ag interactions occur with at least one component in solution (e.g., SPR assays) and thus in 3D conditions. In the case of T lymphocytes, the consequences of these two biophysical conditions on receptor–ligand interactions have been analyzed to some extent. Experiments (15, 16) and mathematical models (7) show that the effective kinetic rates of TCR–ligand interactions obtained in 3D conditions cannot predict the effective kinetic rates obtained in 2D conditions. Moreover, it was also shown that it is the 2D kinetics, not the 3D kinetics, that correlate with Ag potency to activate T cells (36, 37). The theoretical analysis of TCR–ligand interactions was general enough to apply to the cases of BCR–Ag and Ab–Ag interactions (8), but until now, it was not possible to derive quantitative implications for the relationship between 2D BCR–Ag and 3D Ab–Ag interactions. This was due to a lack of quantitative biophysical data on the different modes of rotational diffusion of paratopes in BCRs and Abs. Here, we have

extended our previous work by performing a detailed theoretical analysis of available data on the whole molecule, Fab tilt and Fab twist rotations, which allowed us to obtain quantitative estimates of the global on and off rotational rates of BCR and Ab paratopes.

To determine the parametric dependence of the different on and off paratope rotational rates on the structural properties of both BCRs and Abs, we have used the Narrow Escape Theory (18) and First Passage Processes (19). We have characterized every step entailing the rotational degrees of freedom so that we could use the most precise available empirical estimates of Fab–Fab and Fab–Fc angles and of mean rotational correlation times corresponding to the three rotations considered here. Based on our calculations, there are noticeable variations in the 2D Fab tilt on rates (inverse of τ_t^{2D+}) among the various IgG subclasses, as seen in Fig. 2. It is worth noting that the flexibility of Fab arms in relation to Fc is inversely correlated with the Fab tilt on rate in IgG subclasses. IgG1 and IgG2b have the fastest and slowest tilt on rates, respectively. This implies that differences in hinge structure may provide certain binding advantages to certain IgG subclasses over others. However, the observed differences in Fab tilt on rates are relatively small (in the most favorable scenario, around 55% for $\delta = 2°$ and 66% for $\delta = 19°$); so if this rotation rate contributes to a binding advantage of one isotype over others, it must be a subtle one. Our estimates are based on limited and scattered empirical data on angle ranges and mean rotational correlation times for different Ig isotypes from a few mammal species and were obtained using molecular preparations that inadequately represent BCRs in the 2D condition. As a result, it would be greatly beneficial to conduct new targeted experimental studies on the mean rotational correlation times of BCR and Ab Fab tilt and alignment rotations for various Ig isotypes using current methodologies. These studies will significantly enhance our current estimates and provide greater clarity regarding the role of hinge flexibility in the kinetics of BCR–Ag and Ab–Ag interactions.

Having derived quantitative values for the translational and rotational rates of paratopes enabled us to calculate the thresholds of the intrinsic k^+ rate in 2D and 3D conditions, beyond which $k_{\text{eff}}^+(2D)$ and $k_{\text{eff}}^+(3D)$ approach fast a plateau, as well as the actual values of these plateaus. In particular, the plateau for $k_{\text{eff}}^+(3D)$ is fast approached for values of the intrinsic molecular on rate $k^+ > 10^9\,s^{-1}$ (Fig. 3, *Left*). Although currently there are no experimental data of BCR–Ag interactions with which to compare the theoretical plateau for $k_{\text{eff}}^+(2D)$, we could put to test the theoretical plateau we obtained for $k_{\text{eff}}^+(3D)$ by comparing it with a rather comprehensive sample of monoclonal Abs anti-PhOx provided in ref. 33. The *Lower* and *Upper* uncertainty limits of the theoretical $k_{\text{eff}}^+(3D)$ plateau are, respectively, $\sim 10^8$ and $\sim 10^9\,M^{-1}s^{-1}$ (respectively, dashed red and blue lines in Fig. 3). Strikingly, the *Lower* plateau limit of the theoretical $k_{\text{eff}}^+(3D)$ uncertainty band (gray area in Fig. 3) is in quite good agreement with the highest $k_{\text{eff}}^+(3D)$ empirical values of the monoclonal Abs obtained from primary to tertiary immune responses to PhOx (Fig. 3, *Right*), which lends strong support to our approach. Nevertheless, a wider sample of different sets of monoclonal Abs against different Ags will determine the generality or limitations of our approach. Yet, perhaps more surprising, and with deeper practical implications discussed below, is that the expected effective on and off rate ratios $k_{\text{eff}}^+(2D)/k_{\text{eff}}^+(3D)$ and $k_{\text{eff}}^-(2D)/k_{\text{eff}}^-(3D)$ can be estimated as a function of $k_{\text{eff}}^+(3D)$ (Fig. 4). This is highly relevant because the 2D effective rate constants are the actual ones that determine B cell behavior. Thus, we have uncovered that for values $k_{\text{eff}}^+(3D) > 10^6\,M^{-1}s^{-1}$, both $k_{\text{eff}}^+(3D)$ and k_{eff}^-3D become bad estimators of the corresponding 2D effective constant rates (Fig. 4, vertical pink, dashed lines).

Although our modeling approach does not yield a lower limit for $k_{\text{eff}}^-(2D)$ (and $k_{\text{eff}}^-(3D)$) different from zero, it indicates that for $k^+ > 5 \times 10^6\,s^{-1}$, $k_{\text{eff}}^-(2D) \approx \left(\frac{k_d^- e^-}{k_d^- + e^+}\right)_{2D} \frac{k^-}{k^+} \leq \frac{k^-}{10}\,s^{-1}$. Based on the internalization kinetics of BCR–Ag complexes, it has been argued that since the half-life of the endocytic process is about 0.5 h (or $\approx$ 2000 s), only effective off rates higher than the inverse of that half-life can be subject to selection during affinity maturation in GCs (38). If we now consider this physiologic limit, then for $k^+ > 5 \times 10^6\,s^{-1}$, the following relationship holds: $\frac{1}{2000}\,s^{-1} < k_{\text{eff}}^-(2D) < \frac{k^-}{10}\,s^{-1}$. Therefore, this physiologic limit implies that for $k^+ > 5 \times 10^6\,s^{-1}$, only intrinsic off kinetic rates $k^- > 5 \times 10^{-3}\,s^{-1}$ would be subject to selection.

It is somewhat surprising that despite the widespread use of the seminal works by Berg and Purcell (1) and De Lisi (17), there has been put so little emphasis on the understanding of the biophysics of the molecular interactions of the two central actors in the humoral immune response, BCRs, and Abs, with their cognate Ags. Our present calculations aim to stimulate experimental studies to establish the validity of the uncovered differences between effective BCR–Ag and Ab–Ag binding kinetics and to encourage the development of state-of-the-art molecular dynamics simulations and experimental methods to narrow the estimated rates for some of the aforementioned rotational events.

In summary, we have shown here that, contrary to the traditional implicit assumption, the kinetics of BCR–Ag interactions cannot be inferred from those of Ab–Ag interactions but for those with $k_{\text{eff}}^+(3D) \leq 10^6\,M^{-1}s^{-1}$. This has important implications in interpreting observations related to B cell selection in germinal centers, an essential process in T-dependent humoral responses based on the amount of Ag endocytosed by B cells and presented to Tfh cells. For instance, above the thresholds established by our calculations for the $k_{\text{eff}}^+(3D)$ rate (Fig. 4, vertical pink, dashed lines), they become little informative—if at all—with respect to the Ag-binding strength sensed by a germinal center B cell, and hence on the amount of Ag it can endocytose. In other words, for Abs with $k_{\text{eff}}^+(3D) > 10^6\,M^{-1}s^{-1}$, it cannot be inferred that the germinal center B cells that produced those Abs were selected because they had a higher $k_{\text{eff}}^+(2D)$ rate (or a lower $k_{\text{eff}}^-(2D)$ rate) than B cells producing Abs with 10-fold lower $k_{\text{eff}}^+(3D)$ rates (or 10-fold higher $k_{\text{eff}}^-(2D)$ rates). We must be aware that, paraphrasing Malissen and Bongrand (39), a B cell can make decisions based only on parameters it senses, not on quantities measured in vitro by experimentalists. In this respect, the present results only concern one of two aspects usually neglected in current views of the Ab affinity maturation process and the selective process(es) that lead to it. The other neglected aspect is the role of naturally generated tensile forces acting on Ag-bound BCRs, which can alter to a significant extent the intrinsic unbinding rate k^-, similar to what has been shown for TCRs (40). This second aspect of the BCR–Ag interactions should also be experimentally and theoretically studied.

Data, Materials, and Software Availability. All study data are included in the article and/or *SI Appendix*. The simulation's code is available in the public repository https://github.com/mariocastro73/First-Passage (41).

ACKNOWLEDGMENTS. This work has been partially funded by MCIN/AEI/10.13039/501100011033, through Grants PID2019-106339GB-I00, PID2022-140217NB-I00, and PRE2020-092274, and by "ESF Investing in your future," and by Xunta de Galiza under project GRC-ED431C 2020/02.

Author affiliations: [a]Instituto de Investigación Tecnológica and Grupo Interdisciplinar de Sistemas Complejos, Universidad Pontificia Comillas, Madrid E28015, Spain; [b]Area of Immunology, Faculty of Biology, and Centro de Investigaciones Biomédicas (Biomedical Research Center), Universidade de Vigo, Vigo 36310, Spain; and [c]Instituto Gulbenkian de Ciência, Oeiras 2781-901, Portugal

1. H. C. Berg, E. M. Purcell, Physics of chemoreception. *Biophys. J.* **20**, 193–219 (1977).
2. J. Punt, S. Stranford, P. Jones, J. Owen, *Kuby Immunology* (Macmillan Education, New York, ed. 8, 2019).
3. K. H. Roux, L. Strelets, T. E. Michaelsen, Flexibility of human IgG subclasses. *J. Immunol.* **159**, 3372–3382 (1997).
4. A. Szakal, M. Kosco, J. Tew, A novel in vivo follicular dendritic cell-dependent iccosome-mediated mechanism for delivery of antigen to antigen-processing cells. *J. Immunol.* **140**, 341–353 (1988).
5. B. A. Heesters *et al*., Endocytosis and recycling of immune complexes by follicular dendritic cells enhances b cell antigen binding and activation. *Immunity* **38**, 1164–1175 (2013).
6. W. R. Heath, Y. Kato, T. M. Steiner, I. Caminschi, Antigen presentation by dendritic cells for B cell activation. *Curr. Opin. Immunol.* **58**, 44–52 (2019).
7. J. Faro, M. Castro, C. Molina-París, A unifying mathematical framework for experimental TCR-pMHC kinetic constants. *Sci. Rep.* **7**, 46741 (2017).
8. J. Faro, M. Castro, Affinity selection in germinal centers: Cautionary tales and new opportunities. *Cells* **10**, 1040 (2021).
9. G. I. Bell, Models for the specific adhesion of cells to cells. *Science* **200**, 618–627 (1978).
10. M. Dembo, B. Goldstein, Theory of equilibrium binding of symmetric bivalent haptens to cell surface antibody: Application to histamine release from basophils. *J. Immunol.* **121**, 345–353 (1978).
11. B. Goldstein, R. Griego, C. Wofsy, Diffusion-limited forward rate constants in two dimensions. Application to the trapping of cell surface receptors by coated pits. *Biophys. J.* **46**, 573–586 (1984).
12. B. Goldstein, A. Perelson, Equilibrium theory for the clustering of bivalent cell surface receptors by trivalent ligands. Application to histamine release from basophils. *Biophys. J.* **45**, 1109–1123 (1984).
13. F. D. Batista, D. Iber, M. S. Neuberger, B cells acquire antigen from target cells after synapse formation. *Nature* **411**, 489–494 (2001).
14. M. L. Dustin, S. K. Bromley, M. M. Davis, C. Zhu, Identification of self through two-dimensional chemistry and synapses. *Annu. Rev. Cell Dev. Biol.* **17**, 133–157 (2001).
15. J. Huppa *et al*., TCR-peptide-MHC interactions in situ show accelerated kinetics and increased affinity. *Nature* **463**, 963–967 (2010).
16. J. Huang *et al*., The kinetics of two dimensional TCR and pMHC interactions determine T cell responsiveness. *Nature* **464**, 932–936 (2010).
17. C. Delisi, The effect of cell size and receptor density on ligand-receptor reaction rate constants. *Mol. Immunol.* **18**, 507–511 (1981).
18. D. Holcman, Z. Schuss, Stochastic narrow escape in molecular and cellular biology. *Anal. Appl.* **48**, 108–112 (2015).
19. S. Redner, *A Guide to First-Passage Processes* (Cambridge University Press, 2001).
20. Y. Wu, J. Vendome, L. Shapiro, A. Ben-Shaul, B. Honig, Transforming binding affinities from three dimensions to two with application to cadherin clustering. *Nature* **475**, 510–513 (2011).
21. J. N. Arnold, M. R. Wormald, R. B. Sim, P. M. Rudd, R. A. Dwek, The impact of glycosylation on the biological function and structure of human immunoglobulins. *Annu. Rev. Immunol.* **25**, 21–50 (2007).
22. E. O. Saphire *et al*., Contrasting IgG structures reveal extreme asymmetry and flexibility. *J. Mol. Biol.* **319**, 9–18 (2002).
23. G. Å. Løset, K. H. Roux, P. Zhu, T. E. Michaelsen, I. Sandlie, Differential segmental flexibility and reach dictate the antigen binding mode of chimeric IgD and IgM: Implications for the function of the B cell receptor. *J. Immunol.* **172**, 2925–2934 (2004).
24. N. Wrigley, E. Brown, J. Skehel, Electron microscopic evidence for the axial rotation and inter-domain flexibility of the fab regions of immunoglobulin G. *J. Mol. Biol.* **169**, 771–774 (1983).
25. R. Wade, J. Taveau, J. Lamy, Concerning the axial rotational flexibility of the fab regions of immunoglobulin G. *J. Mol. Biol.* **206**, 349–356 (1989).
26. J. Schlessinger, Lateral and rotational diffusion of EGF-receptor complex: Relationship to receptor-mediated endocytosis. *Biopolymers* **22**, 347–353 (1983).
27. X. Zhang *et al*., 3D structural fluctuation of IgG1 antibody revealed by individual particle electron tomography. *Sci. Rep.* **5**, 9803 (2015).
28. A. Casadevall, A. Janda, Immunoglobulin isotype influences affinity and specificity. *Proc. Natl. Acad. Sci. U.S.A.* **109**, 12272–12273 (2012).
29. N. de Haan, D. Falck, M. Wuhrer, Monitoring of immunoglobulin N- and O-glycosylation in health and disease. *Glycobiology* **30**, 226–240 (2020).
30. D. Lauffenburger, J. Linderman, *Receptors: Models for Binding, Trafficking, and Signaling* (Oxford University Press, USA, 1996).
31. B. Treanor *et al*., The membrane skeleton controls diffusion dynamics and signaling through the B cell receptor. *Immunity* **32**, 187–199 (2010).
32. W. M. Saltzman, M. L. Radomsky, K. J. Whaley, R. A. Cone, Antibody diffusion in human cervical mucus. *Biophys. J.* **66**, 508–515 (1994).
33. J. Foote, C. Milstein, Kinetic maturation of an immune response. *Nature* **352**, 530–532 (1991).
34. F. D. Batista, M. S. Neuberger, Affinity dependence of the B cell response to antigen: A threshold, a ceiling, and the importance of off-rate. *Immunity* **8**, 751–759 (1998).
35. K. Suzuki, I. Grigorova, T. G. Phan, L. M. Kelly, J. G. Cyster, Visualizing B cell capture of cognate antigen from follicular dendritic cells. *J. Exp. Med.* **206**, 1485–1493 (2009).
36. L. J. Edwards, V. I. Zarnitsyna, J. D. Hood, B. D. Evavold, C. Zhu, Insights into T cell recognition of antigen: Significance of two-dimensional kinetic parameters. *Front. Immunol.* **3**, 86 (2012).
37. C. Zhu, N. Jiang, J. Huang, V. I. Zarnitsyna, B. D. Evavold, Insights from in situ analysis of TCR-pMHC recognition: Response of an interaction network. *Immunol. Rev.* **251**, 49–64 (2013).
38. J. Foote, H. N. Eisen, Kinetic and affinity limits on antibodies produced during immune responses. *Proc. Natl. Acad. Sci. U.S.A.* **92**, 1254–1256 (1995).
39. B. Malissen, P. Bongrand, Early T cell activation: Integrating biochemical, structural, and biophysical cues. *Annu. Rev. Immunol.* **33**, 539–561 (2015).
40. B. Liu, W. Chen, B. D. Evavold, C. Zhu, Accumulation of dynamic catch bonds between TCR and agonist peptide-MHC triggers T cell signaling. *Cell* **157**, 357–368 (2014).
41. M. C. Ponce, mariocastro73/First-Passage. GitHub. https://github.com/mariocastro73/First-Passage. Deposited 29 June 2022.